**Author for correspondence:**
Nicholas J. R. Hunter,
E-mail: nicholas.hunter@monash.edu

# Crystallographic preferred orientation (CPO) patterns in uniaxially compressed deuterated ice: quantitative analysis of historical data

Nicholas J. R. Hunter[1] , Christopher J. L. Wilson[1] and Vladimir Luzin[2,3]

[1]School of Earth, Atmosphere and Environment, Monash University, Clayton, VIC 3800, Australia; [2]Australian Centre for Neutron Scattering, Australian Nuclear Science and Technology Organisation, Lucas Heights, NSW 2234, Australia and [3]School of Engineering, The University of Newcastle, Callaghan, NSW 2308, Australia

## Abstract

Strain, temperature and strain rate are crucial factors governing the development of crystallographic preferred orientations (CPO) in ice. To better understand how CPO patterns change in response to these variables, we performed quantitative analyses on neutron diffraction data between 2010 and 2019, collected in situ during uniaxial compression experiments on deuterium ice. At strains >10% and temperatures <−10°C, the *c*-axis pattern switches from a single maximum ('cluster') to small circle ('cone'), both oriented parallel to shortening. The diameter and mean width of the cone pattern decrease as strain and/or strain rate increases. Prismatic axis (*a* and *m*) patterns are characterised by great circles parallel to the pole figure margin and may be distinguishable from the patterns in ice deformed under simple shear. While strain has the main influence on the degree of preferred orientation (or CPO 'strength'), both temperature and strain rate have minor influences, which limits the extent to which CPOs can be used to measure strain. As cluster patterns can be observed in the *c*-axes of ice deformed under both pure and simple shear settings, this may complicate interpretations of flow geometry in terrestrial ice unless the prismatic axis patterns are also considered.

## Introduction

Flow behaviour in terrestrial ice sheets is intimately linked to the mechanical properties of the ice mass, which in part are governed by crystallographic preferred orientations (CPOs; also described in the literature as 'fabric', 'lattice preferred orientation' or 'texture') in the polycrystalline framework. In addition to CPO development, the flow rates of ice sheets are enhanced by changes in grain size, the magnitude of strain and temperature (Budd and Jacka, 1989). Many studies of ice-sheet mechanics assume that differential changes in viscosity are primarily due to CPO development (Azuma, 1994; van der Veen and Whillans, 1994; Morland and Staroszczyk, 2009; Hruby and others, 2020). Indeed recent deformation experiments by Fan and others (2021*a*) suggest that CPO development predominantly governs strain weakening in ice samples. Modelling works from Rathmann and Lilien (2021) show enhancement (which they attribute solely to CPO) must be accounted for in order to accurately infer basal friction of ice masses. In order to understand the constitutive flow laws in a viscously anisotropic material such as natural water ice (Duval and others, 1983) and its deuterium (D$_2$O) analogue (Wilson and others, 2020) there are synergies if we compare CPOs identified in drill cores (Gow and others, 1997; Thorsteinsson and others, 1997) with observations from laboratory experiments.

It is well accepted that precipitation of snow on ice-sheet surfaces induces a vertical flattening at upper regions of the sheet, with the ice deforming mainly by compression along the vertical direction (Alley, 1988). At greater depth, the deformation changes toward bedrock-parallel flow (Budd and Jacka, 1989; Hudleston, 2015). In the majority of ice cores drilled from the surface to intermediate depths there are corresponding changes in the CPO of the (0001) or '*c*-axis' in ice, from a randomly oriented distribution at the surface to a non-random or 'preferred' orientation at depth (Fig. 1) (Gow and others, 1968; Gow and Williamson, 1976; Gow and Weeks, 1977; Gow and Kohnen, 1978, 1979; Kohnen and Gow, 1979; Hudleston, 1980; Weeks and Gow, 1980; Faria and others, 2014). The spatial variation in CPO patterns in ice cores are generally in good agreement with our wider understanding of ice-sheet mechanics at depth, and are therefore considered to be a promising macroscopic flow indicator (Alley, 1992). When combined with the ice microstructure and independent temperature measurements, these CPO patterns may be used to estimate the rheological changes in the flow of ice sheets (Gow and others, 1997; Thorsteinsson and others, 1997; Azuma and others, 1999), or to decipher historical flow events (Dansgaard and others, 1969; Thwaites and others, 1984; Budd and Jacka, 1989; Thorsteinsson and others, 2003; Donoghue and Jacka, 2009; Wilson and Peternell, 2011; Lilien and others, 2021). The Schmid factors can also be incorporated into a CPO-based flow law (Azuma, 1994).

There are, however, some variations in the *c*-axis CPO patterns that form. In many cases, the *c*-axis poles may orient parallel with the loading axis to form a cluster (Herron and others, 1985; Gow and Meese, 2007; Faria and others, 2014). In other cases, a small circle of poles
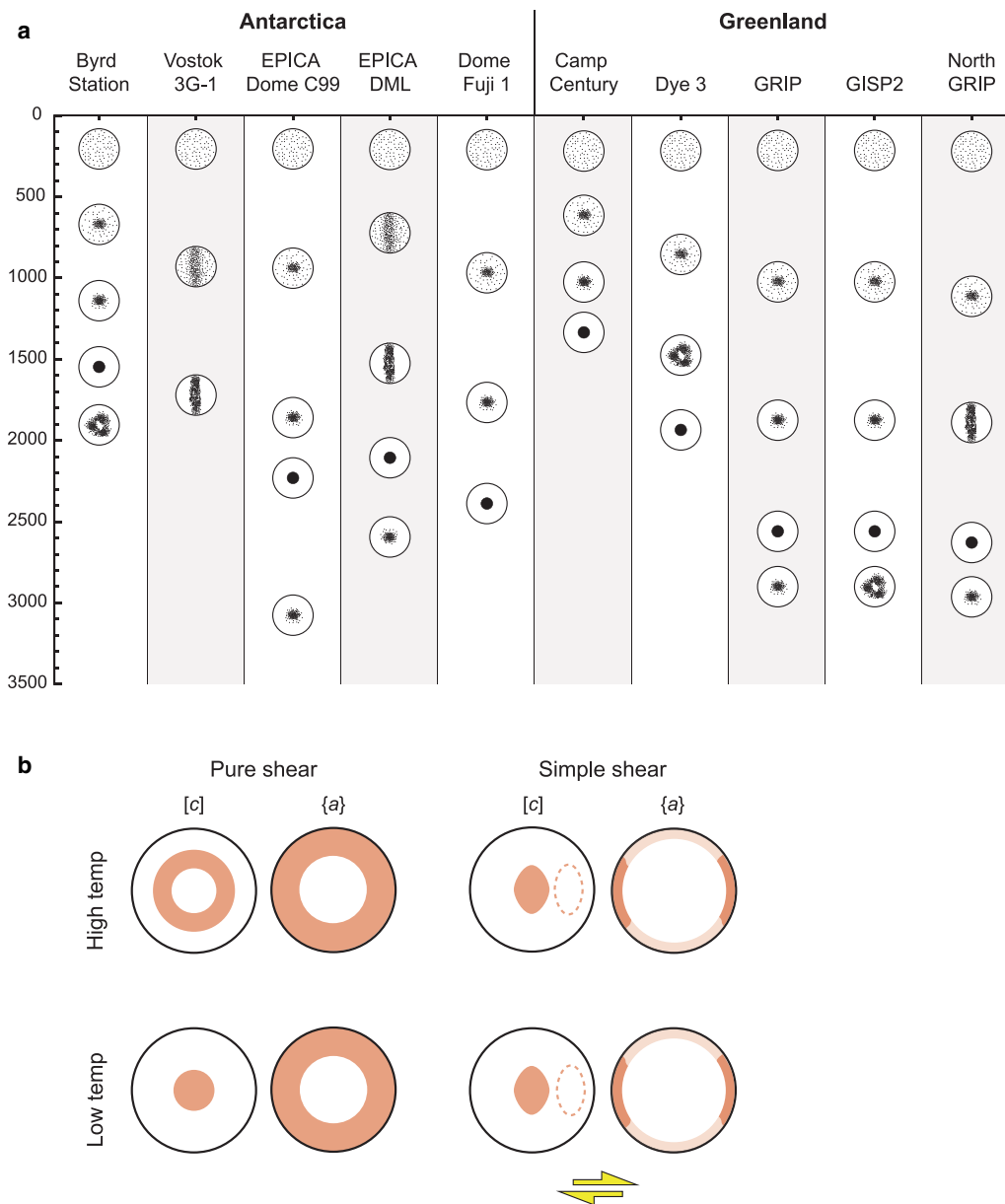
**Fig. 1.** Common CPO patterns in ice. (a) Empirical CPO observations from ice cores (001 axis only). Modified from Faria and others (2014). (b) Synthesis of common CPO patterns from both natural and experimental studies (refer text for references).

about the axis of ice loading, typically referred to as an 'open cone' or 'cone', will develop at greater depths (Gow and Williamson, 1976; Thorsteinsson and others, 1997; Azuma and others, 1999; Faria and others, 2014). Other workers have observed a great circle oriented normal to shortening or 'vertical girdle' (Lipenkov and others, 1989; Wang and others, 2002). The variations in the *c*-axis CPO patterns, and the depth at which they occur, are by no means systematic across the range of ice cores studied (Fig. 1; Faria and others, 2014). Moreover, the empirical evidence from the natural ice record offers only the end-product and cannot inform us of the physical conditions that controlled the observed pattern, let alone an explanation for the differences in CPO patterns across various ice cores. This means that, in general, more work is required to fully understand the array of CPOs in terrestrial ice, and the physical conditions that influence the commonly observed patterns (Fan and others, 2021a).

Controlled experimental deformations in the laboratory have provided important insights into the physical determinants for these patterns (Kamb, 1972; Bouchez and Duval, 1982; Wilson,

1982; Jacka and Maccagnan, 1984; Montagnat and others, 2015; Qi and others, 2017; Wilson and others, 2020). Historically, the majority of studies have employed uniaxial compression experiments, where the compression direction is parallel to the sample shortening axis (Fig. 2b). Most of these studies have found that, when deformed, the initially random *c*-axes of ice samples will preferentially align in a cone centred around the compression axis (Wilson, 1982; Piazolo and others, 2013; Qi and others, 2017). Additional insights into *c*-axis CPO development with a cone-like distribution, in a pure shear environment, are also provided by the power law models of Azuma (1994), which considers the Schmid factor for basal slip in ice crystals as part of its calculations.

When ice samples are uniaxially compressed at temperatures below −20°C and at strains between 8 and 20%, characteristic of many terrestrial ice environments, the *c*-axis cones become tighter and may often take the form of a cluster (Fan and others, 2020, 2021b). A similar cluster pattern may emerge with increased stress (Qi and others, 2017). The transition from cone- to cluster-shaped *c*-axis distributions suggests many ice basal-planes rotate
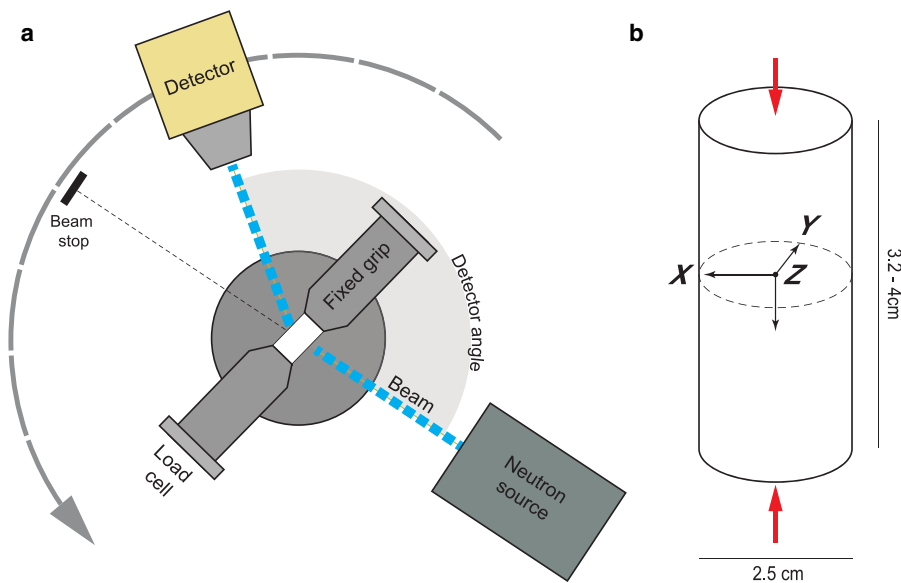
**Fig. 2.** (a) Experimental set-up for combined axial compression deformation and in situ CPO acquisition using neutron diffraction. (b) Orientation of $D_2O$ samples during deformation experiments. Red arrows signify the shortening axis.

from easy (basal) to hard-glide slip orientations (Wilson and others, 2014).

Combining experimental and natural CPO observations, there is some general consistency in the *c*-axis patterns but uncertainty elsewhere (Fig. 1b). Firstly, ice that is experimentally deformed under simple shear conditions typically develop a cluster of *c*-axes aligned parallel with shortening axis at high shear strains ($\gamma > 2$); as they do in low-temperature uniaxial deformations (Bouchez and Duval, 1982; Journaux and others, 2019). At lower strains, a second maximum is commonly observed at a low angle to the shear plane, together forming a 'double-cluster' *c*-axis pattern (dashed lines in Fig. 1b) (Bouchez and Duval, 1982; Journaux and others, 2019; Qi and others, 2019). The angle between these two clusters has been shown to decrease with higher strains (Qi and others, 2019). In the former of these cases, there is an ambiguity when interpreting the cluster-bearing *c*-axis patterns observed in ice core records, given that experiments suggest they form under low-temperature pure shear or high strain simple shear (Fig. 1a).

A second uncertainty is that it is unclear whether the *c*-axis CPO patterns previously interpreted as cones in ice cores are in fact collections of clusters oriented about the shortening axis or 'multi-maxima' (Gow and Williamson, 1976; Tison and Hubbard, 2000; Monz and others, 2021). Both these circumstances mean that it may be difficult to interpret the deformation histories from the *c*-axis CPO patterns observed in ice cores and, moreover, to draw meaningful insights about ice mechanics.

Our incomplete understanding here is due in part to the limitations of methods in previous studies. Many historical studies in ice cores employed a universal stage to obtain measurements of *c*-axis orientations. As this procedure is time- and labour-intensive, and often performed on coarse-grained samples, only a small sample of orientations were collected per study (Gow and Williamson, 1976; Gow and others, 1997; Thorsteinsson and others, 1997). As a result, the maximum tends to be over-estimated and hard to quantify. Furthermore, there is no information on other important crystal axes, such as the prismatic (*a* and *m*) axes, which may also be important kinematic indicators (Schmid and Casey, 1986). Contemporary methods, such as electron backscatter diffraction or 'cryo-EBSD' (Prior and others, 2015), are capable of producing much larger datasets, while also measuring the complete crystal orientation and the grain microstructure. However, there remains some limitation when studying coarse-grained ice samples, which is a common characteristic of high-temperature ($>-10°C$)

deformations where grain boundary migration is a dominant recrystallisation mechanism (Monz and others, 2021).

Experiments involving in situ neutron diffraction offer a solution. This bulk technique allows non-destructive measurement of textures as a function of applied load while acquiring 3-D data in samples up to 250 cm³ in volume. The technique can therefore return CPO data of high-statistical quality, even from very coarse-grained samples (Wenk, 2006; Hunter and others, 2017b). Unfortunately, combining deformation experiments with in situ neutron diffraction is time-intensive and only a small number of individual samples can typically be measured within the project timeframe. However, by combining data from multiple studies, provided that the experimental set-up is consistent, we can leverage the strong sampling power of the neutron diffraction technique, while gaining insights about the sensitivity of ice, in terms of its CPO pattern, to a wider array of strains, temperatures and strain rates.

$D_2O$ ice is used as a proxy for ice because of its transparency for neutrons, which is not the case for $H_2O$. Single-crystal studies have found no significant structural difference between $D_2O$ and $H_2O$ (Peterson and Levy, 1957) and both materials have similar mechanical properties and deformation behaviour (McDaniel and others, 2006; Middleton and others, 2017).

In this contribution, we combine and synthesise nearly a decade of existing experimental data by performing detailed quantitative analyses of the CPO patterns. The data presented here is a secondary analysis of data from coupled in situ deformation and texture diffraction experiments performed at the Australian Nuclear Science and Technology Organisation (ANSTO) in Sydney, Australia between 2010 and 2019. Our primary aim is to investigate the physical conditions that lead to cluster and cone pattern development in the *c*-axis during uniaxial compression of ice. At a high level, we aim to strengthen the gap between experimental and natural insights of these common *c*-axis topologies, and the physical conditions that influence their development. In particular, we will emphasise how the findings inform the interpretation of ice CPO patterns in terrestrial ice.

## Methods

### Experimental deformations

Most data presented in this contribution have been published elsewhere (Piazolo and others, 2013; Wilson and others, 2019, 2020), but are briefly described here for context. Cylindrical

samples of $D_2O$ were deformed in an Instron 100 kN load frame while in situ neutron diffraction measurements were being performed on the residual stress diffractometer *KOWARI* at ANSTO (Fig. 2a) (Kirstein and others, 2009). All experiments were unconfined and conducted under uniaxial compression loading conditions. In all cases, neutron diffraction data were collected after the deformation experiment using a two-circle Eulerian goniometer. All data used in this study represent the final microstructure of the deformed sample.

The samples investigated in this study are composed of polycrystalline $D_2O$ ice prepared using the technique described by Wilson and others (2019). The average length and diameter of $D_2O$ samples were ~3.2–4 cm × 2.5 cm for a length to diameter

ratio of ~1.5 to 1 (Fig. 2b). The testing took place in a chamber that controls the temperature to within ±0.2°C.

The initial dataset comprised of 54 samples (Table 1). Three constant displacement rates and starting strain rates were used across the experimental data: $1 \times 10^{-5}$ s$^{-1}$ ('fast'), $2.5 \times 10^{-6}$ s$^{-1}$ ('medium') and $6.0 \times 10^{-7}$ s$^{-1}$ ('slow'). The temperatures ranged from −3°C to −20°C, and strains ranged from 0 to 40% shortening. The melting temperature ($T_m$) of $D_2O$ ice is +3.8°C. This means that experimentally deforming $D_2O$ in a temperature range of −10°C to −1°C (0.92–0.99$T_m$) corresponds to a $H_2O$ ice temperature range of −13.8°C to −4.8°C (0.95–0.986$T_m$). The temperature and strain rates used across these experiments were chosen due to their approximation with natural ice

**Table 1.** Quantitative summary of deformed ice sample characteristics

| Sample | Temp. °C | Strain rate s−1 | Strain | Second phase content | CtC | Cone colatitude° | Pattern observed | J-index | Texture entropy | Eigenvalue 1 | Eigenvalue 2 | Eigenvalue 3 |
|---|---|---|---|---|---|---|---|---|---|---|---|---|
| 13_17 | – | – | 0.00 | | 1.43 | 66 | Cluster | 1.0067 | −0.0035 | 0.3224 | 0.3349 | 0.3427 |
| 13_24 | – | – | 0.00 | | 1.43 | 84 | Cluster | 1.2038 | −0.0801 | 0.3926 | 0.3261 | 0.2813 |
| MD14 | −7 | $1.00 \times 10^{-5}$ | 0.05 | | 1.20 | 54 | Cluster | 1.0058 | −0.0031 | 0.3311 | 0.3283 | 0.3406 |
| MD21 | −7 | $1.00 \times 10^{-5}$ | 0.05 | | 1.02 | 40 | Cluster | 1.0086 | −0.0044 | 0.3577 | 0.3194 | 0.3229 |
| 13_32B | −7 | $1.00 \times 10^{-5}$ | 0.10 | | 1.21 | 25 | Cluster | 1.034 | −0.0169 | 0.3895 | 0.3081 | 0.3025 |
| 13_26 | −10 | $1.00 \times 10^{-5}$ | 0.10 | | 1.17 | 24 | Cluster | 1.0487 | −0.0245 | 0.2943 | 0.3084 | 0.3973 |
| 13_S1 | −10 | $1.00 \times 10^{-5}$ | 0.10 | | 0.00 | 0 | Cluster | 1.2043 | −0.0944 | 0.2631 | 0.2669 | 0.47 |
| D5-2 | | $2.50 \times 10^{-6}$ | 0.00 | 0.2 | 1.16 | 66 | Cluster | 1.0192 | −0.0096 | 0.3464 | 0.3344 | 0.3192 |
| 13_22 | −10 | $2.50 \times 10^{-6}$ | 0.10 | | 1.13 | 24 | Cluster | 1.0337 | −0.0169 | 0.392 | 0.3024 | 0.3056 |
| MD8 | −7 | $2.50 \times 10^{-6}$ | 0.10 | | 1.05 | 23 | Cluster | 1.0227 | −0.0111 | 0.3116 | 0.3081 | 0.3804 |
| GG_04 | −7 | $2.50 \times 10^{-6}$ | 0.10 | 0.4 | 1.05 | 38 | Cluster | 1.0149 | −0.0077 | 0.3619 | 0.3194 | 0.3187 |
| D2-2 | −7 | $2.50 \times 10^{-6}$ | 0.20 | | 1.73 | 22 | Cluster | 1.3046 | −0.1582 | 0.4843 | 0.2549 | 0.2608 |
| FFC_03 | −7 | $1.00 \times 10^{-5}$ | 0.10 | 0.4 | 0.94 | 27 | Cone | 1.0746 | −0.0374 | 0.4133 | 0.2942 | 0.2925 |
| MD12 | −7 | $1.00 \times 10^{-5}$ | 0.10 | | 0.92 | 35 | Cone | 1.2194 | −0.113 | 0.4653 | 0.2677 | 0.267 |
| 13_30 | −3 | $1.00 \times 10^{-5}$ | 0.10 | | 0.00 | 36 | Cone | 1.2446 | −0.1264 | 0.2615 | 0.2719 | 0.4667 |
| MD15 | −10 | $1.00 \times 10^{-5}$ | 0.20 | | 0.95 | 24 | Cone | 1.4218 | −0.216 | 0.5214 | 0.2369 | 0.2417 |
| FC_01 | −7 | $1.00 \times 10^{-5}$ | 0.20 | 0.2 | 0.94 | 24 | Cone | 1.3875 | −0.1978 | 0.5147 | 0.2404 | 0.2449 |
| MD23 | −10 | $1.00 \times 10^{-5}$ | 0.20 | | 0.87 | 32 | Cone | 1.3744 | −0.1982 | 0.5091 | 0.2438 | 0.2471 |
| G_02 | −7 | $1.00 \times 10^{-5}$ | 0.20 | 0.2 | 0.78 | 37 | Cone | 1.1813 | −0.0933 | 0.4476 | 0.2754 | 0.2769 |
| CC_06 | −7 | $1.00 \times 10^{-5}$ | 0.20 | 0.2 | 0.00 | 34 | Cone | 1.4307 | −0.2179 | 0.516 | 0.2446 | 0.2394 |
| MD7 | −7 | $1.00 \times 10^{-5}$ | 0.20 | | 0.00 | 28 | Cone | 1.8748 | −0.4077 | 0.5778 | 0.2041 | 0.218 |
| MD4 | −7 | $1.00 \times 10^{-5}$ | 0.20 | | 0.00 | 37 | Cone | 1.6683 | −0.2227 | 0.5078 | 0.2467 | 0.2455 |
| MD22 | −7 | $1.00 \times 10^{-5}$ | 0.40 | | 0.00 | 30 | Cone | 2.4356 | −0.718 | 0.6552 | 0.1748 | 0.1699 |
| 13_21 | −10 | $2.50 \times 10^{-6}$ | 0.10 | | 0.98 | 27 | Cone | 1.0882 | −0.0446 | 0.4197 | 0.2922 | 0.2881 |
| DH_28 | −15 | $2.50 \times 10^{-6}$ | 0.10 | | 0.88 | 21 | Cone | 1.4029 | −0.2079 | 0.5136 | 0.2392 | 0.2472 |
| MDCC1 | −7 | $2.50 \times 10^{-6}$ | 0.10 | 0.2 | 0.87 | 36 | Cone | 1.1959 | −0.1004 | 0.461 | 0.272 | 0.267 |
| MDCC2 | −7 | $2.50 \times 10^{-6}$ | 0.10 | 0.2 | 0.84 | 36 | Cone | 1.2845 | −0.1478 | 0.482 | 0.261 | 0.257 |
| MD10 | −7 | $2.50 \times 10^{-6}$ | 0.10 | | 0.81 | 32 | Cone | 1.3752 | −0.1938 | 0.5085 | 0.2415 | 0.2499 |
| MDG4 | −7 | $2.50 \times 10^{-6}$ | 0.10 | 0.2 | 0.00 | 37 | Cone | 1.3149 | −0.1659 | 0.2539 | 0.2602 | 0.4859 |
| 13_20 | −3 | $2.50 \times 10^{-6}$ | 0.10 | | 0.00 | 32 | Cone | 1.2584 | −0.1288 | 0.4621 | 0.2643 | 0.2737 |
| LDH_35 | −7 | $2.50 \times 10^{-6}$ | 0.20 | 0.1 | 0.97 | 37 | Cone | 1.1189 | −0.0602 | 0.4277 | 0.2877 | 0.2846 |
| GG_03 | −7 | $2.50 \times 10^{-6}$ | 0.20 | 0.4 | 0.94 | 35 | Cone | 1.1253 | −0.064 | 0.4279 | 0.2878 | 0.2844 |
| DH_26 | −15 | $2.50 \times 10^{-6}$ | 0.20 | | 0.94 | 24 | Cone | 1.3875 | −0.1978 | 0.5194 | 0.2342 | 0.2464 |
| DH_24 | −20 | $2.50 \times 10^{-6}$ | 0.20 | | 0.87 | 34 | Cone | 1.2745 | −0.1435 | 0.4856 | 0.2548 | 0.2596 |
| D1-7 | −7 | $2.50 \times 10^{-6}$ | 0.20 | | 0.71 | 35 | Cone | 1.4142 | −0.2161 | 0.508 | 0.2477 | 0.2443 |
| FFC_04 | −7 | $2.50 \times 10^{-6}$ | 0.20 | 0.4 | 0.69 | 28 | Cone | 1.2352 | −0.1156 | 0.4669 | 0.2645 | 0.2686 |
| LDH_20_1 | −7 | $2.50 \times 10^{-6}$ | 0.20 | | 0.66 | 39 | Cone | 1.3125 | −0.1634 | 0.4582 | 0.2657 | 0.276 |
| D1-5 | −3 | $2.50 \times 10^{-6}$ | 0.20 | | 0.66 | 33 | Cone | 1.4087 | −0.2123 | 0.5079 | 0.2528 | 0.2393 |
| D5-5 | −7 | $2.50 \times 10^{-6}$ | 0.20 | 0.2 | 0.58 | 36 | Cone | 1.4946 | −0.259 | 0.2369 | 0.2405 | 0.5226 |
| MD9 | −10 | $2.50 \times 10^{-6}$ | 0.20 | | 0.56 | 36 | Cone | 1.7278 | −0.3853 | 0.5711 | 0.2166 | 0.2123 |
| CC_05 | −7 | $2.50 \times 10^{-6}$ | 0.20 | 0.2 | 0.00 | 35 | Cone | 1.4786 | −0.2401 | 0.5204 | 0.236 | 0.2436 |
| FC_07 | −7 | $2.50 \times 10^{-6}$ | 0.20 | 0.2 | 0.00 | 31 | Cone | 1.3362 | −0.1669 | 0.495 | 0.2503 | 0.2547 |
| MDG1 | −10 | $2.50 \times 10^{-6}$ | 0.20 | 0.2 | 0.00 | 38 | Cone | 1.2694 | −0.1409 | 0.4743 | 0.2618 | 0.264 |
| D1-1 | −1 | $2.50 \times 10^{-6}$ | 0.20 | | 0.00 | 36 | Cone | 1.8501 | −0.4427 | 0.5726 | 0.2055 | 0.222 |
| DH_06 | −7 | $2.50 \times 10^{-6}$ | 0.20 | | 0.00 | 36 | Cone | 1.6709 | −0.3461 | 0.5483 | 0.2327 | 0.219 |
| DH_29 | −7 | $2.50 \times 10^{-6}$ | 0.20 | | 0.00 | 36 | Cone | 1.8931 | −0.4546 | 0.2088 | 0.2184 | 0.5728 |
| LDH_20_2 | −7 | $2.50 \times 10^{-6}$ | 0.20 | | 0.00 | 34 | Cone | 1.4316 | −0.2275 | 0.5085 | 0.2478 | 0.2438 |
| LDH_23 | −7 | $2.50 \times 10^{-6}$ | 0.20 | | 0.00 | 37 | Cone | 1.9004 | −0.4758 | 0.2061 | 0.2246 | 0.5693 |
| MD3 | −7 | $2.50 \times 10^{-6}$ | 0.20 | | 0.00 | 35 | Cone | 1.8107 | −0.4268 | 0.5718 | 0.2132 | 0.215 |
| MD13 | −3 | $2.50 \times 10^{-6}$ | 0.20 | | 0.00 | 30 | Cone | 2.4246 | −0.7083 | 0.6384 | 0.1823 | 0.1792 |
| D5-3 | −1 | $2.50 \times 10^{-6}$ | 0.40 | 0.2 | 0.00 | 30 | Cone | 2.6468 | −0.7613 | 0.6561 | 0.1693 | 0.1747 |
| D5-4 | −3 | $2.50 \times 10^{-6}$ | 0.40 | 0.2 | 0.00 | 36 | Cone | 2.0912 | −0.5252 | 0.2029 | 0.1948 | 0.6023 |
| D5-1 | −7 | $2.50 \times 10^{-6}$ | 0.40 | | 0.00 | 32 | Cone | 2.1427 | −0.5429 | 0.6087 | 0.1972 | 0.1941 |
| MD6 | −10 | $6.00 \times 10^{-7}$ | 0.10 | | 0.00 | 37 | Cone | 1.4232 | −0.2227 | 0.5078 | 0.2467 | 0.2455 |

Descriptions for the 'cluster-to-cone ratio' (CtC) ratio and 'cone colatitude' are provided in the Supplementary material. The J-indices of sample CPOs were calculated using the method of Bunge (1982). Texture entropy calculations follow the method of Schaeben (1988). The eigenvalues of the c-axis orientation data were derived using the method of Scheidegger (1965).

conditions $(10^{-5}–10^{-10}\,\mathrm{s}^{-1})$ (Paterson, 1977 and references therein; Vaughan, 1993).

Neutron diffraction measurements were performed in situ with the deformation experiments. The method has been described in detail elsewhere (Wilson and others, 2020). Pole figure data used in this contribution are from diffraction measurements taken at the completion of the deformation experiment. In all experiments, three ice diffraction peaks were measured: (002), (100) and (101). The raw diffraction data patterns were fit with Gaussian peaks to remove background intensity and converted to regular $3° \times 3°$ pole figure mesh grids.

### Secondary data analysis

Quantitative analysis of CPO topologies was undertaken using the MTEX toolbox for MATLAB (http://mtex-toolbox.github.io/). MTEX provides a versatile platform for detailed orientation distribution function (ODF) and pole figure analysis, which allows pole figures to be quantitatively analysed with high precision. The three experimental pole figures were used to reconstruct the ODF, using a 'de Vallee Poussin' kernel and 5° half width. In this contribution, all pole figures reconstructed from the ODF are equal-area, lower hemisphere projections.

For this study, we used a collection of novel parametric routines to analyse the characteristic topologies of the deformed specimens. These routines are briefly summarised here, and further detail is provided in the Supplementary material. There exist a number of measurements that quantify the degree of preferred orientation in a given sample (hereafter described as the CPO 'strength'). In this study, we used the *J*-index (Bunge, 1982), texture entropy (Schaeben, 1988) and orientation tensor (Scheidegger, 1965) (Table 1). Both the *J*-index and texture entropy functions calculate strength from the ODF, whereas the orientation tensor is calculated from the eigenvalues of individual axes in their spherical form (i.e. azimuth and plunge). Where feasible, we conducted same-temperature and same-strain analyses to understand the effects of either parameter on the texture strength.

We measured the variation in multiples of uniform distribution around the pole figure, using a modification of the 'intensity spectrum' routines described by Hunter and others (2018). Here, a line transect is made across the entire pole figure (e.g. E–W) at azimuthal angles between 1 and 180°. This provides a 2-D cross section of the multiples of uniform distribution, which can then be visualised on a Cartesian plot. All transects ($n = 180$) were subsequently averaged to define the mean intensity distribution across the pole figure hemispheres. For the analysis of prismatic axes, where a great circle parallel to the pole figure margin is the common pattern (Fig. 2b), we also measured the mean intensity spectrum along a transect oriented parallel with the great circle (i.e. about the Z-axis; Fig. 2b).

We computed two topological parameters for features commonly observed in the *c*-axes of ice CPO patterns. The *cone colatitude* describes the mean plunge angle of cone girdle maxima within the *c*-axis pole figure. The *cluster-to-cone* (CtC) ratio defines the proportional difference in maxima intensity between cluster and cone maxima in the *c*-axis pole figure. This is calculated by detecting two peaks from the mean intensity spectrum: the cluster from peaks at >80° plunge ($P_{cluster}$); and the cone from peaks at <80° plunge ($P_{cone}$). The ratio is subsequently calculated as $P_{cluster}/P_{cone}$, which thus produces a means of distinguishing cluster-dominant (CtC > 1) and cone-dominant (CtC < 1) CPOs. For cone-dominant samples, we quantified the 'cone diameter', the mean angle between the two cone girdle centres; and the 'girdle width', the mean angle between the start and end of the girdle peaks.

## Results

### Changes in c-axis patterns

At strains >10%, or temperatures <−10°C, there is a switch in the *c*-axis pole figure from a shortening-parallel point maximum (cluster) topology to a shortening-parallel small circle (cone) topology (Fig. 3). The transition from cluster to cone in the *c*-axes is a function of both increasing temperature and strain. As shown in the mean intensity spectra (Fig. 4), with increasing strains and temperatures, the samples transit from a weak but dominant single peak at 90°, or the centre of the pole figure, towards two well-defined peaks at 60° and 120°. These data signify the development of clusters and cones in the *c*-axis pole figures, respectively. The characteristic patterns are also captured by the CtC ratio (Fig. 4c). The transition from clusters (CtC > 1) to cones (CtC < 1) has a negative relationship with the CPO strength (Fig. 4c). In other words, cluster patterns are weak whereas cones are well-defined.

Based on the CtC ratio, a total of 12 samples were identified as exhibiting a cluster-dominant *c*-axis pattern. Common physical characteristics of these samples include (1) very low strains (0–10%); and (2) low-to-medium temperatures. No cluster-dominant textures were found in samples deformed at temperatures higher than −10°C. A cluster-dominant texture was found in one sample deformed at 20% strain (D2-2). Only one of the cluster-bearing samples contained second phases (GG_04: 40% graphite). In samples without second phases, there is an increase in the CPO strength with the transition to cone-bearing *c*-axis CPOs (CtC < 1; Fig. 4c).

Great circles are present in the prismatic (110) and (100) pole figures of all samples, regardless of whether the corresponding *c*-axis pattern exhibits a cluster or cone. However, the great circles are substantially more defined in cone-bearing samples (Fig. 5a). The lack of variation in intensity around the great circles (i.e. about the sample's Z-axis; inset in Fig. 5b) demonstrates that there are no characteristic anisotropies within the pattern (Fig. 5b).

### Changes in CPO strength

To test the effects of different physical parameters on the CPO strength, we filtered the dataset to exclude samples with second phases, as it has been established that these can affect the resulting texture strength and, given the purposes of the current study, may produce ambiguous results (Song and Ree, 2007; Herwegh and others, 2011; Hunter and others, 2016; Wilson and others, 2019). We also restricted our analyses to samples deformed at fast and medium strain rate experiments, due to the limited number of samples deformed at slow strain rates.

Our results suggest that CPOs may become stronger with increases in either strain, strain rate or temperature (Fig. 6), with strain having the strongest influence on the CPO strength. The slope of the data in Figure 6a suggests that, for every 10% increase in strain the *J*-index value will increase by 0.3 for medium strain rates, and 0.4 for fast strain rates (Fig. 6c). This demonstrates how faster strain rates also play a role in increasing the CPO strength.

### Changes in c-axis cone patterns

Using pure ice samples that qualified as cone-dominant (CtC < 1), we investigated changes in the cone topologies as a function of the various deformation conditions. Specifically, we quantified the 'cone width', taken as the mean angle across cone girdle; and the 'girdle width', the mean angle between the start and end of the girdle peaks (refer insets in Fig. 7).

In general, both the cone and girdle widths undergo minor decreases as strains increase, but it is less clear how these aspects of the cone are affected by temperature (Fig. 7). A slight decrease in cone width was detected for faster strain rates, from an average
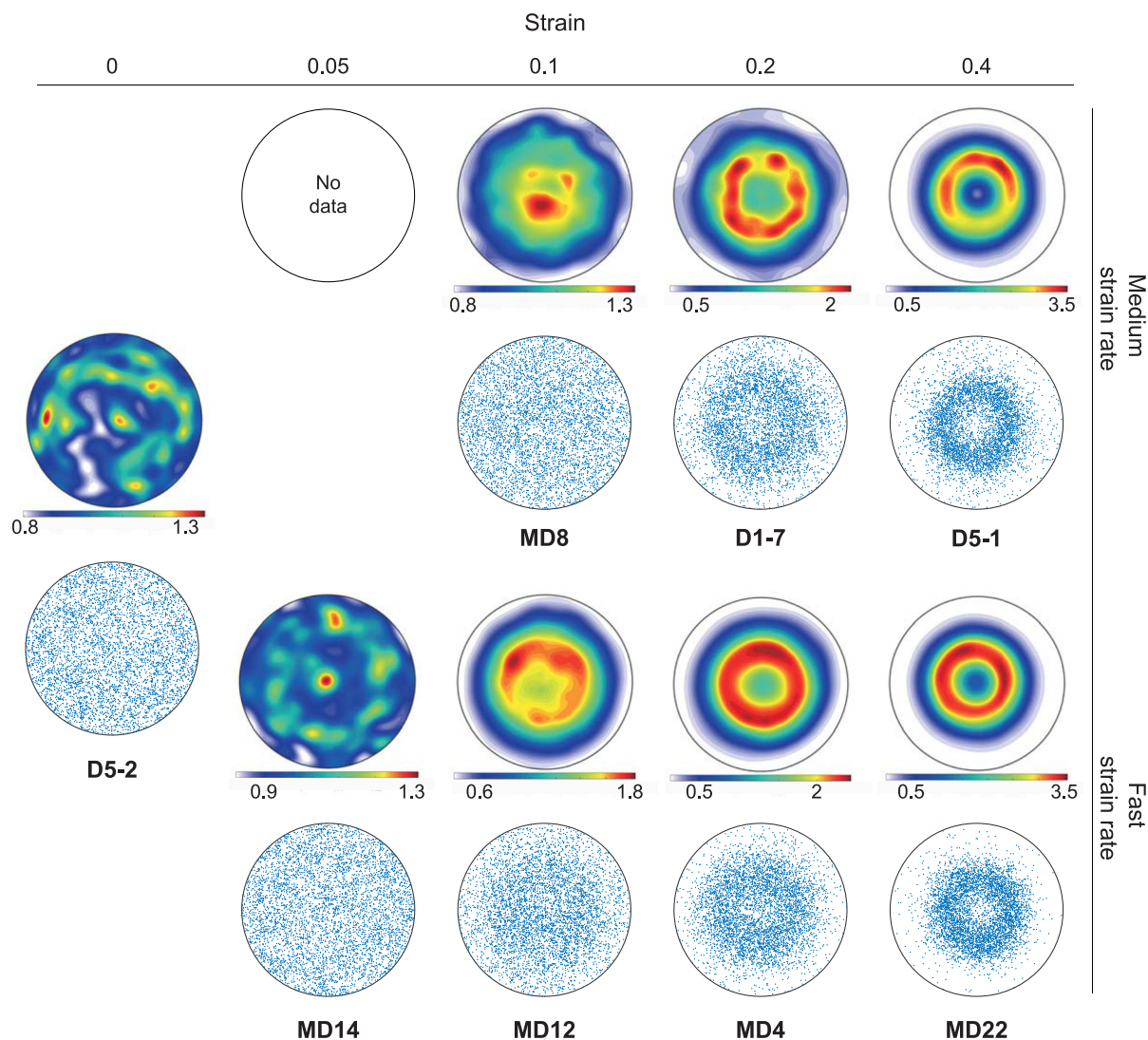
**Fig. 3.** Characteristic *c*-axis CPO patterns for various strains and strain rates. The shortening axis is parallel to the pole figure centre. At zero and low strains, a random distribution characterises the sample. With increased strain, the pattern changes from a weak cluster to a well-defined small circle parallel with the shortening axis, or 'cone'. Point plots were constructed using random orientations (*n* = 10 000) from the ODF.

angle of 70.8° in medium strain rates to 61.6° in faster strain rates. There is a difference of 4.6° per girdle for a magnitude change in strain rate, as thus the effect is negligible.

## Discussion

### From cluster to cone

Combining our data, we have found that, under uniaxial compression and with increasing strain, the *c*-axis CPO typically shifts from a weak cluster to an increasingly sharper cone with narrower width and thinner girdles. This *c*-axis pattern transition is in reasonable agreement with previous experiments (Qi and others, 2017; Fan and others, 2020, 2021*a*) and the decrease in cone width with increasing strain (Fig. 7) is also in agreement with Fan and others (2020).

It is currently accepted that cluster patterns in the *c*-axes of deformed ice are the result of recrystallisation dominated by lattice rotation, whereas cone patterns are developed when recrystallisation is dominated by grain boundary migration (Alley, 1992). The recrystallisation mechanism, in turn, is controlled by the physical conditions. The switch in deformation mechanism from lattice rotation to grain boundary migration recrystallisation, or from cluster to cone in the *c*-axes of ice, typically occurs due to

decreased stress (Qi and others, 2017) or increased temperature (Montagnat and others, 2015).

The development of a *c*-axis cluster parallel to the shortening axis at low strains was observed in partial pole figure data in Piazolo and others (2013) and Wilson and others (2020). Recent uniaxial deformation studies have also found that a *c*-axis cluster may form at low temperatures. For example, Craw and others (2018) observed clusters in several ice samples deformed under uniaxial compression at −30°C, strain rates between $10^{-5}$ and $10^{-6}\,s^{-1}$ and at 20% strain. Fan and others (2020) also observed *c*-axis clusters in ice deformed at the same temperature and strain rate, but across a wider range of strains (8–20%). Data from our study suggest that this cluster development is also possible at warmer temperatures (>−10°C). However, it should be noted that the strength of these patterns is very weak (Fig. 4c).

The question then arises as to why a cluster pattern typically observed in low-temperature deformations was found in several of our high-temperature uniaxial compression experiments, which has been seldom recognised elsewhere (Kamb, 1972; Budd and Jacka, 1989; Wilson and others, 2014). It is possible that lattice rotation played a complementary role in some samples, resulting in the formation of a cluster component. Due to its high-statistical power, neutron diffraction is capable of detecting pole figure components that may not be identified using other
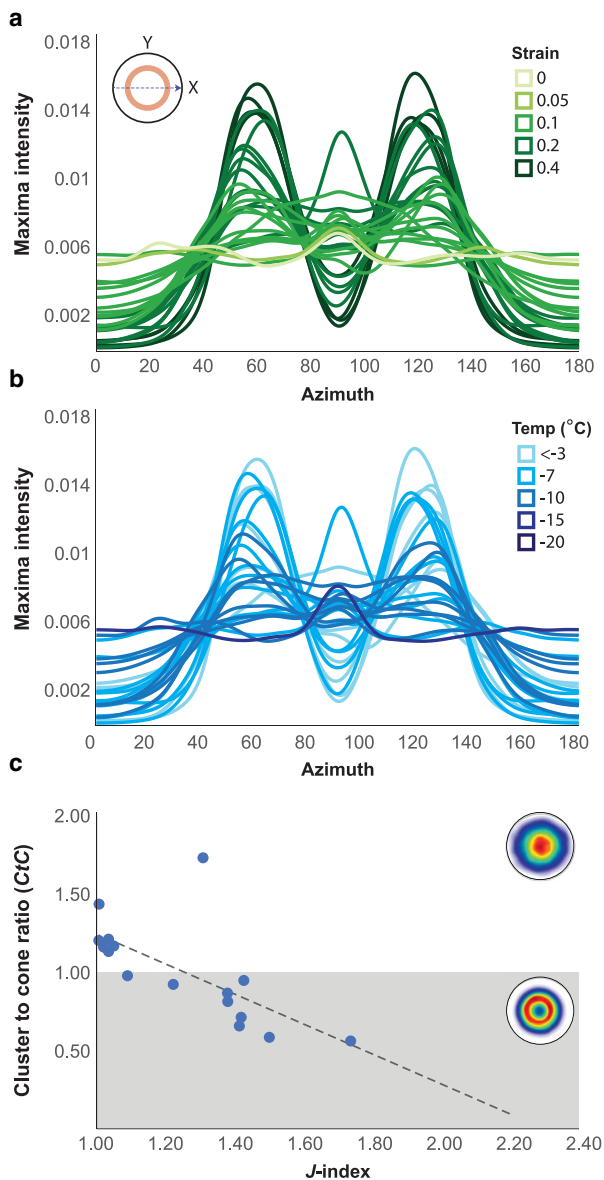
**Fig. 4.** (a) Mean intensity spectra of samples along the or E–W (X) plane of the pole figure (refer blue arrow in the inset), categorised as a function of strain. With increasing strain, the samples transition from a weak but dominant single peak at 90° (cluster), towards two well-defined peaks at 60° and 120° (cone). (b) Mean intensity spectra of samples, following the same rationale as in (a) but categorised as a function of temperature. (c) CtC ratio compared with the CPO intensity ($J$-index).

methods, such as EBSD (Hunter and others, 2017*a*). Given the very low CPO strength of cluster-bearing samples ($J$-indices: 1–1.3) it is possible that these components have not been previously recognised by other methods. Moreover, the low CPO strength of these cluster-bearing samples implies that they are not as well-developed as they are at lower temperatures (Craw and others, 2018; Fan and others, 2020). A more detailed investigation into our subset of cluster-bearing $c$-axis CPOs will form the basis of a future study.

### *From experiments to nature*

We will now place these results in the context of terrestrial ice bodies. A well-developed understanding of changes in ice CPO patterns is important for: (1) interpreting the palaeoconditions from CPO patterns in terrestrial ice; and (2) understanding the rheology of natural ice masses. Furthermore, it is essential to understand the sensitivity of CPO patterns to changes in physical

conditions, which provide a window into the critical strains and temperatures involved in terrestrial ice flow.

In this section, we intend to provide an overview of the implications our results have for interpreting CPO patterns, and the deformation implications, in terrestrial ice. Before embarking on this discussion, it is helpful to separate two elements of the CPO: (1) the pattern itself (cluster or cone in the $c$-axis); and (2) the strength and definition of the pattern. If we are to group these phenomena with respect to their determinants, the pattern observed in the CPO is a function of the deformation regime (e.g. pure or simple shear) and the physical conditions; whereas its strength and definition is only controlled by the physical conditions.

We first discuss the two patterns observed and their implications for interpreting ice flow in nature. We then focus on the definition of the patterns, and the sensitivity of CPOs to changes in physical conditions, with the aim of critically appraising their use as indicators of the natural deformation conditions.

### *Resolving the 'cone problem'*

The transition from cluster to cone can occur due to both strain and temperature (Figs 4a, b, respectively). This represents a shift in the dominant deformation mechanism from the rotation of basal slip planes to an orientation perpendicular to shortening (dislocation glide), to pervasive consumption of grains with low Schmid factors (migration recrystallisation; grain boundary migration) (Hudleston, 2015; Qi and others, 2017).

The development of cones under uniaxial compression is consistent with decades of deformation experiments (Jacka and Li, 2000; Wilson and Sim, 2002; Piazolo and others, 2013). Despite this, relatively few cones are observed in terrestrial ice cores (Faria and others, 2014). Moreover, the poor data quality for the low number of cone observations raises the question of whether these $c$-axis CPOs are in fact groups of clusters ('multi-maxima') depicting several flow events (Monz and others, 2021). These issues raise questions about the existence of cones in nature.

If we assume that the cones previously observed in ice cores are, in fact, groups of clusters then this introduces further uncertainties when trying to understand flow behaviour. Clusters are the commonly observed pattern in ice samples deformed experimentally under simple shear (Qi and others, 2019), so a tempting interpretation is that cluster-bearing ice cores may reflect widespread simple shear conditions. However, our data show that a cluster-based $c$-axis CPO may also form under pure shear settings, as observed in other uniaxial compression experiments (Craw and others, 2018; Fan and others, 2020). Moreover, the data here adds further ambiguity by demonstrating that cluster-bearing $c$-axis patterns in ice deformed under pure shear are not restricted to cold temperatures (<−20°C) as previously shown (Fan and others, 2020); this pattern may also form, albeit weakly, in under warmer temperatures (>−10°C). There is, thus, an even wider range of deformation conditions under which this pattern may emerge, and it is possible that we are still far from understanding the full spectrum.

In many cases, the CPO of ice cores is determined through seismic reflection methods (Vélez and others, 2016; Vaughan and others, 2017; Lutz and others, 2020) and only the $c$-axis can be quantified. If we are to properly understand the flow behaviour of natural ice masses, namely the deformation regime, an additional pole figure should be inspected.

Our experimental data suggest that, when viewed in two dimensions parallel to the pole figure margin, there is a common great circle topology in the prismatic $a$- and $m$-axes (Fig. 5). Prismatic axes in simple sheared ice, by contrast, exhibit strongly anisotropic patterns, developing strong maxima that bear a relationship with the shear direction (Fig. 1b) (Journaux and others, 2019; Qi and others, 2019; Monz and others, 2021). These differences in the
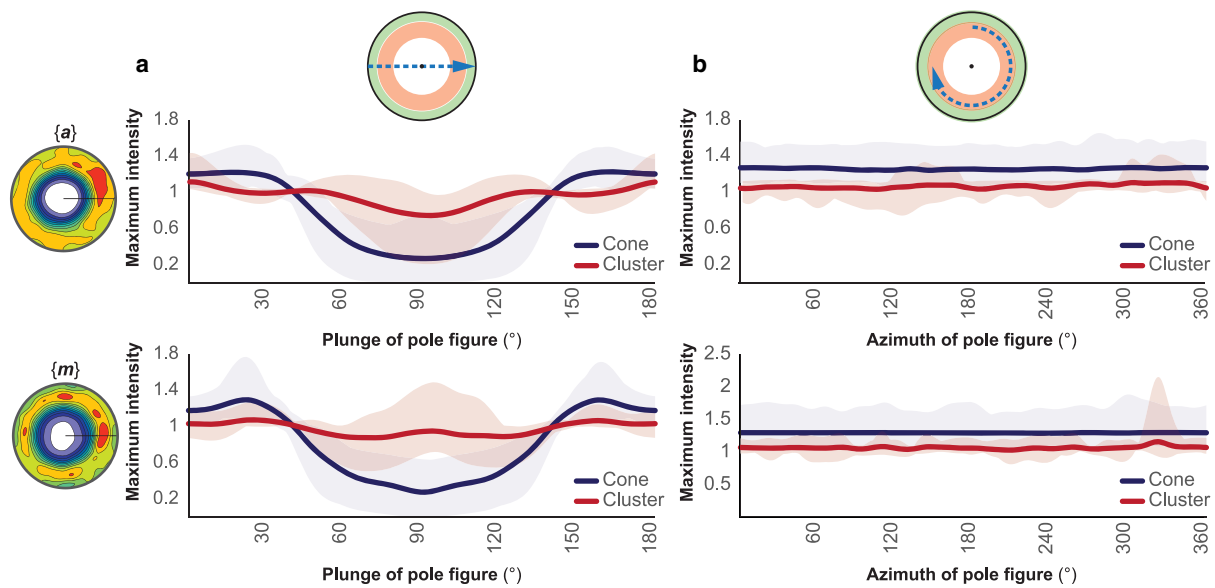
**Fig. 5.** Characteristic prismatic (110) and (100), or '*a*' and '*m*', patterns in ice samples, plotted using mean intensity spectra. The blue arrows in pole figure insets represent the directions from which intensity data were taken. (a) Mean intensity spectra for (110) and (100) collected E–W of the pole figure. In both pole figures, the mean intensity spectra for cone samples (blue lines) exhibit two peaks close 0° and 180°, characteristic of a great circle at the pole figure margin. Mean intensity spectra for cluster sample are flat, due to their weakness of the overall CPO. (b) Mean intensity spectra for (110) and (100) collected around the maximum in each pole figure (about the sample's *Z*-axis, as defined in Fig. 2b). In most cases, the mean intensity spectrum is flat, indicating no distinct anisotropies.
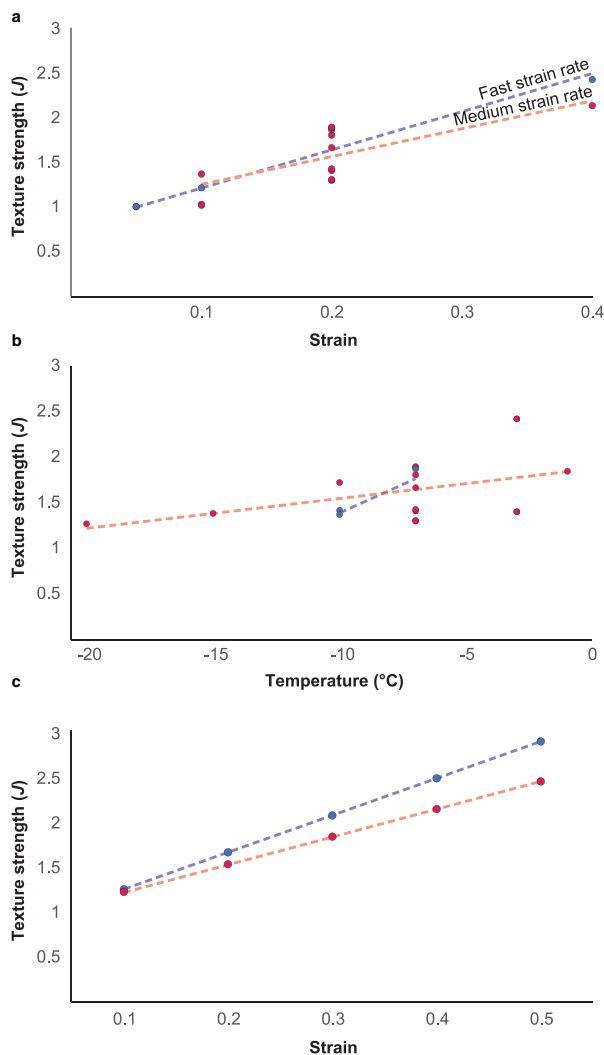


**Fig. 6.** Relationships between CPO intensity (measured by *J*-index) and changes in (a) strain (temperature: −7°C), and (b) temperature (strain: 20%). (c) Sensitivity of *J*-index to strain, based on slopes in (a). Two strain rates (fast: blue line; medium: red line) are presented for comparison.

prismatic pole figures highlight a potential for better distinguishing the deformation regime when a cluster-based pattern is observed in the *c*-axis pole figure of natural ice specimens.

Another possibility for differentiating between pure and simple shear conditions is to apply the 'crystal vorticity axis' (CVA) method of (Michels and others, 2015). Under this method, vorticity is determined by isolating the crystallographic orientations inside individual grains and measuring their rotational distribution to calculate a dispersion axis. When measured across multiple grains in the sample the average dispersion axis, or vorticity axis, can then be used to determine pure and simple shear components. The CVA method has recently been applied to grains in an ice core from Priestley Glacier and, combined with CPO data, were used to resolve the deformation geometry (Thomas and others, 2021).

It is also notable that, under simple shear conditions, the cluster pattern developed in the *c*-axis pole figure takes a more elliptical form compared to the more circular patterns developed under pure shear (Fig. 1). Where shear strains are lower a second maximum at a low angle to the shear plane may also be present (Journaux and others, 2019; Qi and others, 2019). While these subtle differences may not be distinguishable in the *c*-axis CPO of ice cores, it is nonetheless an observation that may aid the interpretation of data.

### Effectiveness of CPO strength as a strain indicator

As with other plastically deforming minerals, such as olivine and quartz, our ability to diagnose deformation events from their naturally developed CPOs is still limited. CPO development is controlled by a combination of physical or 'extrinsic' factors (strain, strain rate, temperature) and 'intrinsic' factors (e.g. pinning from second phases) (Hunter and others, 2019). A common belief, though not confirmed unequivocally, is that there is a relationship between strain and CPO strength. Indeed, this relationship has been observed in previous ice experiments (Kamb, 1972; Wilson, 1982; Journaux and others, 2019). In the high-temperature and stress ice experiments presented by Fan and others (2021*a*), CPO evolution is able to account for all the observed weakening and not grain size evolution.
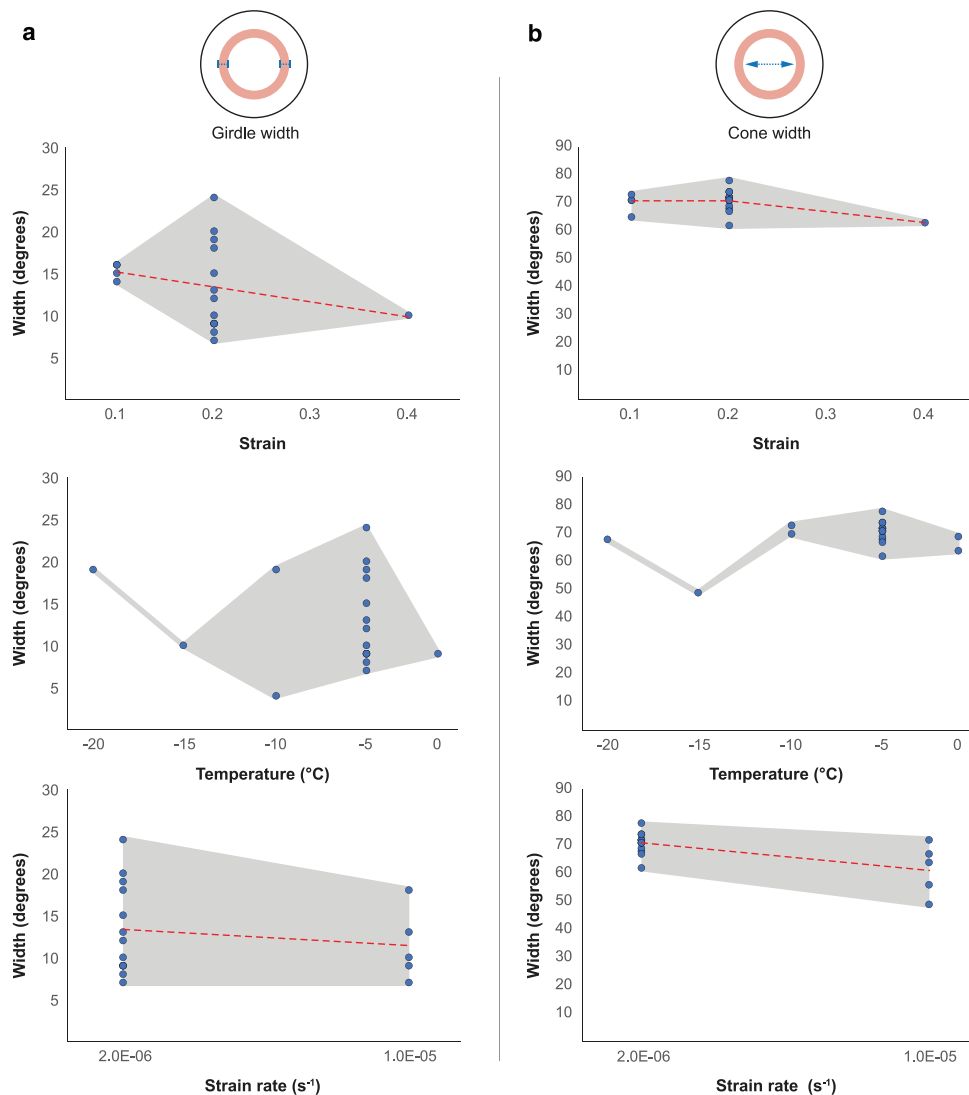
**Fig. 7.** Influence of increased strain, strain rate and temperature on (a) girdle width and (b) cone width. Strain data are from experiments at −7°C. Temperature data are from experiments at 20% strain. Refer insets for visual definitions of girdle and cone widths.

It is therefore tempting to perceive CPOs as a reliable indication of strain, which could potentially be applied to ice and other geological materials. Recent studies on crustal rocks (Larson and others, 2017; Larson, 2018; Starnes and others, 2020) have suggested that the strength of CPO patterns could be used as a strain proxy for resolving shear zone discontinuities in mountain belts. Experimental studies, where physical parameters can be controlled, are useful for corroborating these claims.

In the analysis of the experiments presented here, it is demonstrated that the increasing CPO strength, smaller cone diameters and narrower girdles are mostly due to the strain conditions across the experiments, which conforms with previous studies (Hudleston, 1977; Montagnat and others, 2012). However, our data suggest that temperature and strain rate also influence the strength of the CPO pattern. In Figure 6c, for example, it is shown that $J$-index values, a measurement of CPO strength, are higher for samples deformed at faster strain rates. The influence of strain rate on CPO strength in deuterated ice was also observed in previous studies (Piazolo and others, 2013; Wilson and others, 2019). Across our analyses, we are unable to find a topological change in the CPO that is exclusively sensitive to strain variations. Another parameter not considered in this study is the role of stress on the CPO strength. There is evidence that stress governs the activity of strain-induced grain boundary migration, which in

turn strongly affects CPO development (Fan and others, 2021a). The role of stress in CPO development is relevant to all geological materials and should be the basis of future studies.

While strain clearly has the strongest influence on the CPO strength, we cannot rule out the influences of temperature, strain rate and possibly stress. This underlines the ambiguities when attempting to use CPOs for deciphering deformation conditions. As a result, certain caution must be taken when using the strength of CPOs as a strain approximation in naturally deformed ice and other geological materials.

## Conclusions

We analysed data from coupled in situ $D_2O$ ice deformation and texture diffraction experiments collected between 2010 and 2019 to investigate the physical conditions that lead to changes in CPO patterns. Cluster patterns in the $c$-axis are typically observed at warmer temperatures ($\geqslant-10°C$) and lower strains ($\leqslant 20\%$). These CPOs, albeit low in strength, suggest that a small component of lattice rotation may be active, but this should be confirmed with further microstructural analyses (e.g. EBSD).

Our data complement previous ice studies, which together implies that cluster patterns can be observed in the $c$-axes of ice deformed under both pure and simple shear settings. That the

same pattern can be developed in either deformation setting suggests that there may be ambiguities when interpreting flow behaviour from c-axis CPO patterns in ice cores. However, we observed that prismatic axis (a and m) pole figures share a common pattern under pure shear, characterised by a girdle parallel to the pole figure margin with no clear anisotropies. This contrasts with the highly anisotropic a- and m-axis patterns in ice deformed under simple shear conditions, and thus the prismatic axes may be more useful for deciphering between the two deformation regimes.

With increasing strain (≥20%) and temperature (>−10°C) the c-axis patterns change from a cluster to cone pattern. At higher strains (40%) and faster strain rates ($1 \times 10^{-5}$) the c-axis cone diameters are smaller and the cone girdles are narrower. While strain clearly has the strongest influence on a given sample's degree of preferred orientation, or 'strength', we cannot rule out the influences of temperature, strain rate and possibly stress. This suggests that the CPO strength is governed by a complex array of determinants, and limits the extent to which CPO strength can be used to estimate the deformation conditions in ice and possibly other geological materials.

**Supplementary material.** The supplementary material for this article can be found at https://doi.org/10.1017/jog.2022.95.

## References

**Alley RB** (1988) Fabrics in polar ice sheets: development and prediction. *Science* **240**(4851), 493–495. doi: 10.1126/science.240.4851.493.

**Alley RB** (1992) Flow-law hypotheses for ice-sheet modeling. *Journal of Glaciology* **38**(129), 245–256. doi: 10.1017/S0022143000003658.

**Azuma N** (1994) A flow law for anisotropic ice and its application to ice sheets. *Earth and Planetary Science Letters* **128**(3–4), 601–614. doi: 10.1016/0012-821X(94)90173-2.

**Azuma N and 6 others** (1999) Textures and fabrics in the Dome F (Antarctica) ice core. *Annals of Glaciology* **29**, 163–168. doi: 10.3189/172756499781821148.

**Bouchez JL and Duval P** (1982) The fabric of polycrystalline ice deformed in simple shear: experiments in torsion, natural deformation and geometrical interpretation. *Textures and Microstructures* **5**(3), 171–190. doi: 10.1155/tsm.5.171.

**Budd WF and Jacka TH** (1989) A review of ice rheology for ice sheet modelling. *Cold Regions Science and Technology* **16**(2), 107–144. doi: 10.1016/0165-232X(89)90014-1.

**Bunge HJ** (1982) *Texture Analysis in Materials Science: Mathematical Methods*, 2nd Edn. London: Butterworth-Heinemann.

**Craw L, Qi C, Prior DJ, Goldsby DL and Kim D** (2018) Mechanics and microstructure of deformed natural anisotropic ice. *Journal of Structural Geology* **115**, 152–166. doi: 10.1016/j.jsg.2018.07.014.

**Dansgaard W, Johnsen SJ, Møller J and Langway CC Jr.** (1969) One thousand centuries of climatic record from cAMP century on the Greenland ice sheet. *Science* **166**(3903), 377–380. doi: 10.1126/science.166.3903.377.

**Donoghue S and Jacka T** (2009) The stress pattern within the Law Dome Summit to Cape Folger Ice Flow line, inferred from measurements of crystal fabrics. *Low Temperature Science* **68**(Suppl), 125–135. http://hdl.handle.net/2115/45439.

**Duval P, Ashby MF and Anderman I** (1983) Rate-controlling processes in the creep of polycrystalline ice. *The Journal of Physical Chemistry* **87**, 4066–4074. doi: 10.1021/j100244a014.

**Fan S and 7 others** (2020) Temperature and strain controls on ice deformation mechanisms: insights from the microstructures of samples deformed to progressively higher strains at −10, −20 and −30°C. *The Cryosphere* **14**(11), 3875–3905. doi: 10.5194/tc-14-3875-2020.

**Fan S and 6 others** (2021a) Crystallographic preferred orientation (CPO) development governs strain weakening in ice: insights from high-temperature deformation experiments. *Journal of Geophysical Research: Solid Earth* **126**(12), e2021JB023173. doi: 10.1029/2021JB023173.

**Fan S and 5 others** (2021b) Kinking facilitates grain nucleation and modifies crystallographic preferred orientations during high-stress ice deformation. *Earth and Planetary Science Letters* **572**, 117136. doi: 10.1016/j.epsl.2021.117136.

**Faria SH, Weikusat I and Azuma N** (2014) The microstructure of polar ice. Part I: highlights from ice core research. *Journal of Structural Geology* **61**, 2–20. doi: 10.1016/j.jsg.2013.09.010.

**Gow AJ and 6 others** (1997) Physical and structural properties of the Greenland Ice Sheet Project 2 ice core: a review. *Journal of Geophysical Research: Oceans* **102**(C12), 26559–26575. doi: 10.1029/97JC00165.

**Gow AJ and Kohnen H** (1978) Ultrasonic measurements on deep ice cores from Antarctica. *Antarctic Journal of the United States* **13**(4), 48–50.

**Gow AJ and Kohnen H** (1979) The relationship of ultrasonic velocities to c-axis fabrics and relaxation characteristics of ice cores from Byrd Station, Antarctica. *Journal of Glaciology* **24**(90), 147–153. doi: 10.1017/S0022143000014702.

**Gow AJ and Meese D** (2007) Physical properties, crystalline textures and c-axis fabrics of the Siple Dome (Antarctica) ice core. *Journal of Glaciology* **53**(183), 573–584. doi: 10.3189/002214307784409252.

**Gow AJ, Ueda HT and Garfield DE** (1968) Antarctic ice sheet: preliminary results of first core hole to bedrock. *Science* **161**(3845), 1011. doi: 10.1126/science.161.3845.1011.

**Gow AJ and Weeks WF** (1977) The internal structure of fast ice near Narwhal Island, Beaufort Sea, Alaska. Article, 77-29. Available at http://hdl.handle.net/11681/9500.

**Gow AJ and Williamson T** (1976) Rheological implications of the internal structure and crystal fabrics of the West Antarctic ice sheet as revealed by deep core drilling at Byrd Station. *Geological Society of America Bulletin* **87**(12), 1665–1677. doi: 10.1130/0016-7606(1976)87<1665:RIOTIS>2.0.CO;2.

**Herron SL, Langway Jr. CC and Brugger KA** (1985) Ultrasonic velocities and crystalline anisotropy in the ice core from Dye 3, Greenland. *Greenland Ice Core: Geophysics, Geochemistry, and the Environment* **33**, 23–31.

**Herwegh M, Linckens J, Ebert A, Berger A and Brodhag SH** (2011) The role of second phases for controlling microstructural evolution in polymineralic rocks: a review. *Journal of Structural Geology* **33**(12), 1728–1750. doi: 10.1016/j.jsg.2011.08.011.

**Hruby K and 5 others** (2020) The impact of temperature and crystal orientation fabric on the dynamics of mountain glaciers and ice streams. *Journal of Glaciology* **66**(259), 755–765. doi: 10.1017/jog.2020.44.

**Hudleston PJ** (1977) Progressive deformation and development of fabric across zones of shear in glacial ice. In Saxena S and Bhattacharji S (eds), *Energetics of Geological Processes*. New York: Springer-Verlag, pp. 121–150.

**Hudleston PJ** (1980) The progressive development of inhomogeneous shear and crystallographic fabric in glacial ice. *Journal of Structural Geology* **2**(1–2), 189–196. doi: 10.1016/0191-8141(80)90049-8.

**Hudleston PJ** (2015) Structures and fabrics in glacial ice: a review. *Journal of Structural Geology* **81**, 1–27. doi: 10.1016/j.jsg.2015.09.003.

**Hunter NJR, Hasalová P, Weinberg RF and Wilson CJL** (2016) Fabric controls on strain accommodation in naturally deformed mylonites: the influence of interconnected micaceous layers. *Journal of Structural Geology* **83**, 180–193. doi: 10.1016/j.jsg.2015.12.005.

**Hunter NJR, Luzin V and Wilson CJL** (2017b) Direct measurement of the quartz c-axis using neutron diffraction. *Tectonophysics* **712–713**, 464–468. doi: 10.1016/j.tecto.2017.05.019.

**Hunter NJR, Weinberg RF, Wilson CJL and Law RD** (2018) A new technique for quantifying symmetry and opening angles in quartz c-axis pole figures: implications for interpreting the kinematic and thermal properties of rocks. *Journal of Structural Geology* **112**, 1–6. doi: 10.1016/j.jsg.2018.04.006.

**Hunter NJR, Weinberg RF, Wilson CJL, Luzin V and Misra S** (2019) Quartz deformation across interlayered monomineralic and polymineralic rocks: a comparative analysis. *Journal of Structural Geology* **119**, 118–134. doi: 10.1016/j.jsg.2018.12.005.

**Hunter NJ, Wilson CJ and Luzin V** (2017a) Comparison of quartz crystallographic preferred orientations identified with optical fabric analysis,

electron backscatter and neutron diffraction techniques. *Journal of Microscopy* **265**(2), 169–184. doi: 10.1111/jmi.12472.

Jacka T and Li J (2000) Flow rates and crystal orientation fabrics in compression of polycrystalline ice at low temperatures and stresses. In Hondoh T (ed.), *Physics of Ice Core Records*. Hokkaido: Hokkaido University Press, pp. 83–102.

Jacka TH and Maccagnan M (1984) Ice crystallographic and strain rate changes with strain in compression and extension. *Cold Regions Science and Technology* **8**(3), 269–286. doi: 10.1016/0165-232X(84)90058-2.

Journaux B and 6 others (2019) Recrystallization processes, microstructure and crystallographic preferred orientation evolution in polycrystalline ice during high-temperature simple shear. *The Cryosphere* **13**(5), 1495–1511. doi: 10.5194/tc-13-1495-2019.

Kamb B (1972) Experimental recrystallization of ice under stress. *Flow and Fracture of Rocks* **16**, 211–241. doi: 10.1029/GM016p0211.

Kirstein O, Luzin V and Garbe U (2009) The strain-scanning diffractometer Kowari. *Neutron News* **20**(4), 34–36. doi: 10.1080/10448630903241175.

Kohnen H and Gow AJ (1979) Ultrasonic velocity investigations of crystal anisotropy in deep ice cores from Antarctica. *Journal of Geophysical Research: Oceans* **84**(C8), 4865–4874. doi: 10.1029/JC084iC08p04865.

Larson KP (2018) Refining the structural framework of the Khimti Khola region, east-central Nepal Himalaya, using quartz textures and *c*-axis fabrics. *Journal of Structural Geology* **107**, 142–152. doi: 10.1016/j.jsg.2017.12.014.

Larson K, Cottle J, Lederer G and Rai SM (2017) Defining shear zone boundaries using fabric intensity gradients: an example from the east-central Nepal Himalaya. *Geosphere* **13**(3), 771–781. doi: 10.1130/ges01373.1.

Lilien DA, Rathmann NM, Hvidberg CS and Dahl-Jensen D (2021) Modeling ice-crystal fabric as a proxy for ice-stream stability. *Journal of Geophysical Research: Earth Surface* **126**(9), e2021JF006306. doi: 10.1029/2021JF006306.

Lipenkov VY, Barkov NI, Duval P and Pimienta P (1989) Crystalline texture of the 2083 m ice core at Vostok Station, Antarctica. *Journal of Glaciology* **35**(121), 392–398. doi: 10.1017/S0022143000009321.

Lutz F and 9 others (2020) Constraining ice shelf anisotropy using shear wave splitting measurements from active-source borehole seismics. *Journal of Geophysical Research: Earth Surface* **125**(9), e2020JF005707. doi: 10.1029/2020JF005707.

McDaniel S, Bennett K, Durham W and Waddington E (2006) In situ deformation apparatus for time-of-flight neutron diffraction: texture development of polycrystalline ice $I_h$. *Review of Scientific Instruments* **77**, 093902. doi: 10.1063/1.2349603.

Michels ZD, Kruckenberg SC, Davis JR and Tikoff B (2015) Determining vorticity axes from grain-scale dispersion of crystallographic orientations. *Geology* **43**(9), 803–806. doi: 10.1130/g36868.1.

Middleton CA, Grindrod PM and Sammonds PR (2017) The effect of rock particles and $D_2O$ replacement on the flow behaviour of ice. *Philosophical Transactions of the Royal Society A: Mathematical, Physical and Engineering Sciences* **375**(2086), 20150349. doi: 10.1098/rsta.2015.0349.

Montagnat M and 6 others (2012) Measurements and numerical simulation of fabric evolution along the Talos Dome ice core, Antarctica. *Earth and Planetary Science Letters* **357–358**, 168–178. doi: 10.1016/j.epsl.2012.09.025.

Montagnat M and 5 others (2015) Analysis of dynamic recrystallization of ice from EBSD orientation mapping. *Frontiers in Earth Sciences* **3**, 81. doi: 10.3389/feart.2015.00081.

Monz ME and 7 others (2021) Full crystallographic orientation (*c* and *a* axes) of warm, coarse-grained ice in a shear-dominated setting: a case study, Storglaciären, Sweden. *The Cryosphere* **15**(1), 303–324. doi: 10.5194/tc-15-303-2021.

Morland LW and Staroszczyk R (2009) Ice viscosity enhancement in simple shear and uni-axial compression due to crystal rotation. *International Journal of Engineering Science* **47**(11), 1297–1304. doi: 10.1016/j.ijengsci.2008.09.011.

Paterson WSB (1977) Secondary and tertiary creep of glacier ice as measured by borehole closure rates. *Reviews of Geophysics* **15**(1), 47–55. doi: 10.1029/RG015i001p00047.

Peterson SW and Levy HA (1957) A single-crystal neutron diffraction study of heavy ice. *Acta Crystallographica* **10**(1), 70–76. doi: 10.1107/S0365110X5700016X.

Piazolo S, Wilson CJL, Luzin V, Brouzet C and Peternell M (2013) Dynamics of ice mass deformation: linking processes to rheology, texture, and microstructure. *Geochemistry, Geophysics, Geosystems* **14**(10), 4185–4194. doi: 10.1002/ggge.20246.

Prior DJ and 15 others (2015) Making EBSD on water ice routine. *Journal of Microscopy* **259**(3), 237–256. doi: 10.1111/jmi.12258.

Qi C and 8 others (2019) Crystallographic preferred orientations of ice deformed in direct-shear experiments at low temperatures. *The Cryosphere* **13**(1), 351–371. doi: 10.5194/tc-13-351-2019.

Qi C, Goldsby DL and Prior DJ (2017) The down-stress transition from cluster to cone fabrics in experimentally deformed ice. *Earth and Planetary Science Letters* **471**, 136–147. doi: 10.1016/j.epsl.2017.05.008.

Rathmann NM and Lilien DA (2021) Inferred basal friction and mass flux affected by crystal-orientation fabrics. *Journal of Glaciology* **68**(268), 755–765. doi: 10.1017/jog.2021.88.

Schaeben H (1988) Entropy optimization in quantitative texture analysis. *Journal of Applied Physics* **64**(4), 2236–2237. doi: 10.1063/1.341694.

Scheidegger AE (1965) On the statistics of the orientation of bedding planes, grain axes, and similar sedimentological data. *U.S. Geologic Survey Professional Paper* **525-C**, 164–167.

Schmid SM and Casey M (1986) Complete fabric analysis of some commonly observed quartz *c*-axis patterns. *Mineral and Rock Deformation: Laboratory Studies* **36**, 263–286. doi: 10.1029/GM036p0263.

Song WJ and Ree JH (2007) Effect of mica on the grain size of dynamically recrystallized quartz in a quartz-muscovite mylonite. *Journal of Structural Geology* **29**(12), 1872–1881. doi: 10.1016/j.jsg.2007.09.011.

Starnes J, Long S, Gordon S, Zhang J and Soignard E (2020) Using quartz fabric intensity parameters to delineate strain patterns across the Himalayan Main Central thrust. *Journal of Structural Geology* **131**, 103941. doi: 10.1016/j.jsg.2019.103941.

Thomas RE and 11 others (2021) Microstructure and crystallographic preferred orientations of an azimuthally oriented ice core from a lateral shear margin: Priestley Glacier, Antarctica. *Frontiers in Earth Science* **9**, 702213. doi: 10.3389/feart.2021.702213.

Thorsteinsson T, Kipfstuhl J and Miller H (1997) Textures and fabrics in the GRIP ice core. *Journal of Geophysical Research: Oceans* **102**(C12), 26583–26599. doi: 10.1029/97JC00161.

Thorsteinsson T, Waddington ED and Fletcher RC (2003) Spatial and temporal scales of anisotropic effects in ice-sheet flow. *Annals of Glaciology* **37**, 40–48. doi: 10.3189/172756403781815429.

Thwaites RJ, Wilson CJL and McCray AP (1984) Relationship between borehole closure and crystal fabrics in Antarctic ice core from Cape Folger. *Journal of Glaciology* **30**(105), 171–179. doi: 10.1017/S0022143000005906.

Tison JL and Hubbard B (2000) Ice crystallographic evolution at a temperate glacier: Glacier de Tsanfleuron, Switzerland. In Maltman AJ, Hubbard B and Hambrey MJ (eds), *Deformation of Glacial Materials*. London: Geological Society of London, pp. 23–38.

van der Veen CJ and Whillans IM (1994) Development of fabric in ice. *Cold Regions Science and Technology* **22**(2), 171–195. doi: 10.1016/0165-232X(94)90027-2.

Vaughan DG (1993) Relating the occurrence of crevasses to surface strain rates. *Journal of Glaciology* **39**(132), 255–266. doi: 10.3189/S0022143000015926.

Vaughan MJ and 5 others (2017) Insights into anisotropy development and weakening of ice from in situ P-wave velocity monitoring during laboratory creep. *Journal of Geophysical Research: Solid Earth* **122**(9), 7076–7089. doi: 10.1002/2017JB013964.

Vélez JA, Tsoflias GP, Black RA, Van der Veen CJ and Anandakrishnan S (2016) Distribution of preferred ice crystal orientation determined from seismic anisotropy: evidence from Jakobshavn Isbræ and the North Greenland Eemian Ice Drilling facility, Greenland. *Geophysics* **81**(1), WA111–WA118. doi: 10.1190/GEO2015-0154.1.

Wang Y and 5 others (2002) A vertical girdle fabric in the NorthGRIP deep ice core, North Greenland. *Annals of Glaciology* **35**, 515–520. doi: 10.3189/172756402781817301.

Weeks WF and Gow AJ (1980) Crystal alignments in the fast ice of Arctic Alaska. *Journal of Geophysical Research: Oceans* **85**(C2), 1137–1146. doi: 10.1029/JC085iC02p01137.

Wenk HR (2006) Neutron diffraction texture analysis. *Reviews in Mineralogy and Geochemistry* **63**(1), 399–426. doi: 10.2138/rmg.2006.63.15.

Wilson CJL (1982) Fabrics in polycrystalline ice deformed experimentally at −10°C. *Cold Regions Science and Technology* **6**(2), 149–161. doi: 10.1016/0165-232X(82)90007-6.

Wilson CJL, Hunter NJR, Luzin V, Peternell M and Piazolo S (2019) The influence of strain rate and presence of dispersed second phases on the deformation behaviour of polycrystalline $D_2O$ ice. *Journal of Glaciology* **65**(249), 101–122. doi: 10.1017/jog.2018.100.

**Wilson CJL and Peternell M** (2011) Evaluating ice fabrics using fabric analyser techniques in Sørsdal Glacier, East Antarctica. *Journal of Glaciology* **57**(205), 881–894. doi: 10.3189/002214311798043744.

**Wilson CJL, Peternell M, Hunter NJR and Luzin V** (2020) Deformation of polycrystalline D$_2$O ice: its sensitivity to temperature and strain-rate as an analogue for terrestrial ice. *Earth and Planetary Science Letters* **532**, 115999. doi: 10.1016/j.epsl.2019.115999.

**Wilson CJL, Peternell M, Piazolo S and Luzin V** (2014) Microstructure and fabric development in ice: lessons learned from in situ experiments and implications for understanding rock evolution. *Journal of Structural Geology* **61**, 50–77. doi: 10.1016/j.jsg.2013.05.006.

**Wilson CJL and Sim HM** (2002) The localization of strain and *c*-axis evolution in anisotropic ice. *Journal of Glaciology* **48**(163), 601–610. doi: 10.3189/172756502781831034.